



## 2 (S)TEM structural and compositional nanoanalyses of chemically 3 synthesized glutathione-shelled nanoparticles

4 A. M. Beltrán<sup>1</sup> · J. M. Manuel<sup>2,3</sup> · R. Litrán<sup>2,3</sup> · E. Félix<sup>2,3</sup> · A. J. Santos<sup>2,4</sup> · F. M. Morales<sup>2,4</sup> ·  
5 O. Bomati-Miguel<sup>2,3</sup>

6 Received: 11 March 2020 / Accepted: 15 April 2020  
7 © King Abdulaziz City for Science and Technology 2020

### 8 Abstract

9 This work is focused on the characterization by transmission and scanning–transmission electron microscopy-related tech-  
10 niques of core–shell nanoparticles synthesized via chemical methods. Different semiconducting, pure metallic or oxide materi-  
11 als have been utilized as the core (cadmium telluride, gold, magnetite, or magnetite covered with gold) of the nanoparticle,  
12 while they have been, in all cases, functionalized by a thin amorphous glutathione layer, with the goal of using the nanopar-  
13 ticles in biomedical applications such as biomarkers, and computerized tomography and image magnetic resonance contrast  
14 agents. The results show that it is possible to visualize the glutathione layer using spectroscopic and imaging techniques,  
15 associated with electron microscopy (such as energy-dispersive X-ray spectroscopy and high-resolution transmission electron  
16 microscopy images), that this layer is present at the surfaces of all observed nanoparticles, and that it is no thicker than a few  
17 nanometers. Electron microscopy also revealed that the nanoparticles core is crystalline and, in average, around 5-nm size.

18 **Keywords** Nanoparticle · Glutathione · Gold · Magnetite · QD · Electron microscopy

### 19 Introduction

20 Nanoparticles (NPs) are defined as solid aggregates of atoms  
21 which, having different shapes, present dimensions between  
22 1 and 100 nm (Hochella 2002), therefore, they can be con-  
23 sidered a subgroup among the colloidal particles. Although  
24 first described during the Royal Society Bakerian Lecture  
25 of 1857, by Michael Faraday, on the interactions between  
26 light and metals, NPs have been always present in nature and  
27

the human being have been using them, without a clear con-  
science of their existence, for centuries (Griffin et al. 2018).  
Nevertheless, their artificial synthetization, with the pur-  
pose of targeting specific applications, only started in the  
second half of the twentieth century (Birrenbach and Spei-  
ser 1976; Kreuter 2009). The use of NPs is extensive and  
they are employed to develop novel environment-friendly  
techniques, such as chemical mechanical polishing slurries  
with different metals (Zhang et al. 2019, 2020), machining  
methods (Zhang et al. 2015), and diamond wheels (Zhang  
et al. 2012). Thanks to these technologies, ultra-smooth sur-  
faces and high-performance devices are achieved for several  
applications, i.e., semiconductor, microelectronics, and aero-  
space industries, which is extremely difficult to be fabricated  
by traditional machining and manufacturing (Zhang et al.  
2017). The small size of these materials causes effects such  
as quantum confinement, which, in combination with their  
high reactivity due to a high specific surface area, makes  
NP engineering an ideal platform for custom-made func-  
tions, providing solutions for a large amount of disciplines,  
from electronics (Matsui 2005) to biomedicine (Karley et al.  
2011; Ventola 2017; Gheibi Hayat and Darroudi 2019).

Among a large variety of compositions, three types of  
NPs present interesting features for biomedical applications:

A1 ✉ J. M. Manuel  
A2 jose.manuel@uca.es

A3 <sup>1</sup> Department of Ingeniería y Ciencia de los Materiales y del  
A4 Transporte. Escuela Politécnica Superior, Universidad de  
A5 Sevilla, 41011 Sevilla, Sevilla, Spain

A6 <sup>2</sup> IMEYMAT: Institute of Research on Electron Microscopy  
A7 and Materials, University of Cádiz, 11510 Puerto Real,  
A8 Cádiz, Spain

A9 <sup>3</sup> Department of Condensed Matter Physics, Faculty  
A10 of Sciences, University of Cádiz, 11510 Puerto Real, Cádiz,  
A11 Spain

A12 <sup>4</sup> Department of Materials Science and Metallurgic  
A13 Engineering, and Inorganic Chemistry, Faculty of Sciences,  
A14 University of Cádiz, 11510 Puerto Real, Cádiz, Spain

51 gold (Au) NPs, quantum dots (QDs), and magnetic NPs.  
 52 Au NPs have been widely utilized during the last decade in  
 53 medical applications such as drug delivery and diagnosis  
 54 (Kumari et al. 2019; Ramalingam 2019), used as computer-  
 55 ized tomography (CT) contrast agents, and even as therapeutic  
 56 agents in optical hyperthermia. The physical, chemical  
 57 and optical properties of Au NPs, like their surface plasmon  
 58 band (Amendola et al. 2017) and their capability to enhance  
 59 the X-ray attenuation and their low cytotoxicity, make them  
 60 highly attractive to biomedical uses. Magnetite ( $\text{Fe}_3\text{O}_4$ ) is a  
 61 highly interesting material to utilize as NP since it is super-  
 62 paramagnetic at room temperature, and, when certain coat-  
 63 ing is used, its toxicity is reduced, even eliminated. There-  
 64 fore, these types of NPs are ideal contrast agents for medical  
 65 diagnosis via magnetic resonance (MRI). On the other hand,  
 66 semiconductor QDs, such as cadmium telluride (CdTe) NPs,  
 67 offer an interesting tool for biomarkers due to their unique  
 68 size-tunable optical properties and, consequently, their size-  
 69 dependent fluorescence (Le Trequesser et al. 2013). In this  
 70 case, since the toxicity might also be a concern for these  
 71 NPs, they are mostly utilized in ex vivo biomedical diagno-  
 72 sis (Kairdolf et al. 2013).

73 These systems offer another advantage: NPs can be func-  
 74 tionalized and coated with a polymer layer in the sense of  
 75 achieving biomedical applications, such as targeted drug  
 76 deliver, or marker for imaging certain types of cells, thanks  
 77 to a high, specific affinity of such polymer. Glutathione  
 78 ( $\text{C}_{10}\text{H}_{17}\text{N}_3\text{O}_6\text{S}$ , or GSH) is a tripeptide containing a thiol  
 79 group to be linked to the NP surface, as well as both, amino  
 80 and carboxylic groups that remain free to be subsequently  
 81 crosslinked with other biomolecules, as we have previously  
 82 shown (Hong et al. 2006; Kumar et al. 2014). In this work,  
 83 we have used GSH as capping agent for the functionalization  
 84 of four types of NPs: CdTe QDs with potential applications  
 85 as biomarkers, gold NPs with potential applications as CT  
 86 contrast agent, magnetite NPs with potential applications as  
 87 MRI contrast agent, and, finally, gold-magnetite NPs than  
 88 can be used as dual contrast agents for bimodal MRI and CT  
 89 bimodal imaging. In all cases, NPs are “in situ” func-  
 90 tionalized during the synthesis step, using GSH. Achieving a cor-  
 91 rect functionalization process is one of the most important  
 92 goals for potential medical applications that require subse-  
 93 quent crosslinking with specific biomolecules.

94 It has to be taken into account, nevertheless, that, if the  
 95 GSH layer is not properly linked to the NP, undesired results  
 96 (such as the formation of a non-homogenous or a too-thick  
 97 GSH layer) could produce defective NP systems. Therefore,  
 98 to ensure that a proper synthetization has been achieved, a  
 99 complete set of analyses have to be carried out. Such analy-  
 100 ses should not only include chemical techniques, but also  
 101 methods that provide reliable information on the distribution  
 102 of GSH around the NP. Direct visualization of hydrophilic  
 103 molecules in colloidal NP coating layers is possible through

the use of high-cost equipment and complex analyses, such  
 as last-generation electron microscopes or cryogenic-trans-  
 mission electron microscopes. For this reason, researchers  
 on the colloidal NP field commonly chose techniques that  
 yield information on the electric charge of the NPs (such  
 as measurements of zeta potential and isoelectric pH) or  
 on the composition of the coating layers (such as Raman  
 and X-ray photoelectron spectroscopies). However, those  
 methods do not reveal the thickness or the homogeneity of  
 these layers around the NP. Thus, in this work, transmission  
 and scanning–transmission electron microscopy, or (S)TEM,  
 has been chosen as the main tool for the NP–GSH system  
 since it comprehends techniques that join the structural and  
 compositional characterization, with high spatial resolution.  
 Precisely, this is the emphasis of the study: to demonstrate  
 the usefulness of the combination of (S)TEM techniques to  
 properly characterize the GSH layer on NPs. In this sense, in  
 this work, three different GSH-covered NP systems are fully  
 characterized by the use of this microscopy. Since the goal  
 of this work is the characterization of GSH-covered NPs,  
 these systems do not have by themselves a specific bio-func-  
 tionalization; the carboxylic and amino terminal groups in  
 GSH will allow subsequent crosslinking with biomolecules.

## Materials and methods

The nanoparticles of this work, which are schematically  
 illustrated in Fig. 1, were synthesized through different  
 chemical methods and consist of four types of core materi-  
 als, which are, in all cases, covered by a thin GSH layer.  
 Later on, sets of nanoparticles were prepared and labeled,

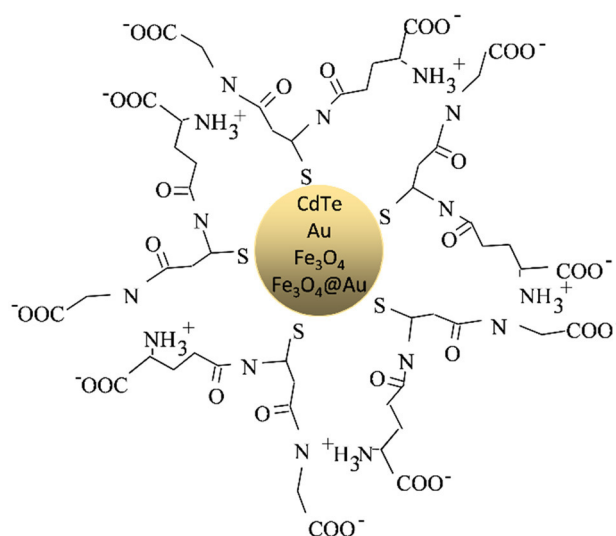


Fig. 1 NP concept, consisting of a core made from one out of four possible materials, and glutathione molecules covering it

133 according to these core materials, as samples S1–S4, which  
 134 were afterwards characterized by means of electron microscop-  
 135 y. In this sense, the label S1 indicates a sample of GSH-  
 136 capped CdTe NPs. The material under the GSH layer in sam-  
 137 ple S2 particles is magnetite. The label S3 is used for the  
 138 sample in which the core is solely formed by gold. Finally,  
 139 sample S4 consists in threefold-material particles: an inner  
 140 Fe<sub>3</sub>O<sub>4</sub> core underneath a thin Au interlayer and a glutathione  
 141 shell at the surface of the NP.

## 142 Synthesis of samples

143 A brief description of the chemical methods to obtain each  
 144 sample is described hereafter. These methods are presented  
 145 in more detail in a different work by the authors focused in  
 146 the application of these materials as biomarkers for medical  
 147 purposes (Beato-López et al. 2012, 2017; Fernández-Ponce  
 148 et al. 2018). Commercial GSH was utilized to obtain the  
 149 coated NP. In all cases, NPs were synthesized at the facilities  
 150 of the Department of Condensed Matter Physics, associated  
 151 with the Institute of Research on Electron Microscopy and  
 152 Materials (IMEYMAT), of the University of Cádiz.

### 153 Synthesis of GSH-capped CdTe NPs (sample S1)

154 The synthesis of GSH–CdTe QDs was carried out in two  
 155 steps, by introducing substantial changes on the methods  
 156 shown in previous reports (Beato-López et al. 2012, 2017).  
 157 First, tellurium (Te) powder was reduced in the presence  
 158 of NaBH<sub>4</sub>, to obtain the Te precursor for QD preparation.  
 159 The GSH–CdTe QDs were prepared by a co-precipitation  
 160 reaction. For this purpose, 0.19 g GSH, used as a stabi-  
 161 lizing agent, and 0.046 g CdCl<sub>2</sub>, used as the cadmium  
 162 (Cd) precursor, were dissolved in 100 ml MQ water. The  
 163 Cd<sup>2+</sup>:NaHTe:GSH molar ratio was 4:1:10. To promote the  
 164 formation of Cd<sup>2+</sup>–GSH complexes at the QD surface, pH  
 165 was adjusted to 8 by dropwise addition of a 1 M NaOH  
 166 solution, under vigorous stirring. The obtained solution was  
 167 placed in a 500-ml three-necked flask, where 2 ml of fresh  
 168 NaHTe (previously prepared in the first step) was added. The  
 169 solution was heated under reflux in a nitrogen atmosphere.  
 170 The final QD sizes can be controlled increasing temperature  
 171 and reaction time.

### 172 Synthesis of GSH-capped magnetite (sample S2)

173 The synthesis of GSH–Fe<sub>3</sub>O<sub>4</sub> NPs was also performed in  
 174 two steps. The first step consists of the preparation of a  
 175 NaOH solution that was used as oxidizing agent for the co-  
 176 precipitation of Fe and formation of Fe<sub>3</sub>O<sub>4</sub>. This solution  
 177 was prepared by heating 20 g of NaOH and 20 ml of dieth-  
 178 ylene glycol at 120 °C for 1 h. After this time, the resulting  
 179 solution is stored at 70 °C for its posterior utilization. The

second step was the main thermal decomposition and co-  
 precipitation reaction. For that, 0.55 g of FeCl<sub>3</sub>, used as iron  
 (Fe) precursor, has been dissolved in 15 ml of diethylene  
 glycol solvent. The obtained solution has been placed in a  
 500-ml three-necked flask, where the GSH used as capping  
 agent has been added. The solution was heated to 200 °C  
 under reflux in a nitrogen atmosphere to promote the ther-  
 mal decomposition of Fe salt. After heating for 30 min, the  
 NaOH solution previously prepared had been added to pro-  
 voke the co-precipitation of Fe and the formation of iron  
 oxide.

### Synthesis of GSH-capped Au NPs (sample S3)

Au NPs were prepared by the reduction of 10 ml of 0.01  
 MAuCl<sub>4</sub> mixed with 10 ml 0.026 M GSH. The mixture was  
 vigorously stirred for 30 min under a nitrogen atmosphere.  
 Then NaBH<sub>4</sub> was added dropwise at 1:5 HAuCl<sub>4</sub>/NaBH<sub>4</sub>  
 molar ratio. After 30 additional minutes, the red wine color  
 solution was stored at 8 °C protected from light. All of them  
 were aqueous solutions.

### Synthesis of GSH–Au magnetite (sample S4)

In this case, GSH–magnetite was added to a solution con-  
 taining HAuCl<sub>4</sub> and GSH in excess to form the Au core over  
 the NPs previously prepared.

## Characterization techniques

Structural and compositional characterizations of all sam-  
 ples have been performed using different (S)TEM-related  
 techniques. Imaging methods such as conventional bright  
 field (BF-TEM), high-resolution (HRTEM) and high-angle  
 annular dark field STEM (HAADF-STEM) allowed to visu-  
 alize structural features, such as size or atomic structure.  
 On the other hand, energy-dispersive X-ray spectrometry  
 (EDX) has been used for subtracting compositions in punc-  
 tual areas, as well as to draw compositional maps of areas  
 ranging from few nm<sup>2</sup> up to μm<sup>2</sup>. Those techniques were  
 applied in three STEM microscopes, supplied by Thermo  
 Fisher Scientific: a double-aberration corrected TITAN<sup>3</sup>  
 Themis and a Talos F200X, both managed by the Central  
 Services of Research, Science and Technology (SC-ICYT,  
 by its initials in Spanish) of the University of Cádiz, and  
 a Talos F200S microscope equipped with Super-X system  
 which includes two silicon drift detectors, which belong to  
 the Research, Technology and Innovation Center of the Uni-  
 versity of Seville (CITIUS). All three of these microscopes  
 were operated at a 200 kV accelerating voltage.

To observe the samples under the electron beam, the  
 chemically obtained NPs were deposited in holey and/or  
 lacey carbon films on copper TEM grids. For that purpose,

NP powders were first dissolved in water at different concentrations or even directly deposited on the grid, with the idea of obtaining the optimal particle concentration for TEM observation. To avoid an excessive amount of magnetic NPs in the grid later entered in the TEM microscope (which uses magnetic field-based lenses), a magnet was moved close to the NP-containing grid before its insertion in the microscope sample holder.

## Results and discussion

### Structural characterization

Depending on the dissolution degree with which the NP powders have been deposited on the TEM grids, it is possible to observe conglomerates of NP of different sizes, as it is presented in Fig. 2, besides isolated NPs. In the case of NPs with magnetic cores (Fig. 2b, d), conglomerates are more frequently detected than in the other cases, due to the magnetic forces among those NPs. Nevertheless, in all cases, it was possible to resolve a statistically significant number of particles to carry out size and compositional quantifications. In this sense, as presented in Table 1, it was possible to determine that the fabrication methods lead to average NP sizes lower than 10 nm. The lower size corresponds to GSH-capped CdTe NP, S1, which explains the difficulty for distinguishing among those NPs in low-magnification images, such as the one presented in Fig. 2a. Note that the carbon supporting structure (“C-support”, in the image), due to its amorphous atomic arrangement, should not appear in

**Table 1** NPs and their core average sizes and GSH maximum thicknesses

Sample	NP core	NP size (nm)	Core size (nm)	GSH max. thickness (nm)
S1	CdTe	$3.9 \pm 1.1$	n.m.	n.m.
S2	$\text{Fe}_3\text{O}_4$	$7.4 \pm 1.0$	$5.0 \pm 0.3$	$0.4 \pm 0.1$
S3	Au	$5.1 \pm 0.7$	$5.1 \pm 0.9$	$2.4 \pm 0.3$
S4	$\text{Fe}_3\text{O}_4@Au$	$6.5 \pm 1.1$	$4.4 \pm 1.0$	$1.1 \pm 0.3$

*n.m.* not measured

HAADF images since it does not produce electron beam diffraction. Nevertheless, it is not uncommon if brightness level is high enough, for these supporting structures to appear in STEM images. In all cases, rounded and spherical-shaped NPs seemed to be predominant, even more in those samples using gold (samples S3 and S4, Fig. 2c, d), although observations using HRTEM, as it will be commented next in the text, reveal cubic-shaped NP crystalline cores, as it was expected.

The phase-contrast TEM mode, also known as high-resolution TEM or HRTEM, reveals areas with a crystalline structure, such as the NPs cores, by presenting atomic columns or fringes, depending on how the crystalline planes diffract the electronic beam emitted by the microscope source. If the material under observation is amorphous, as it is the case of the GSH shell and the carbon matrix supporting the NPs, these images would show a continuous region where the intensity is distributed without any particular order. This allowed (1) to observe the crystalline nature of the NP core and its size [which is an important property of the particle (Kumari et al. 2019)] and (2) to determinate the maximum thickness of the GSH forming the cap layer in these systems. This is also possible thanks to the use of lacey carbon-type grids, in which particles are frequently found at the border of the carbon-web, and thus the carbon signal does not screen the one from the amorphous NP cover along all the particle surface. With this in mind, it was possible to complete Table 1, indicating also the average size of the core in the nanoparticles and the maximum amorphous glutathione cover thickness, for each studied sample. As a complement to this table, Fig. 3 shows the histograms for the measurements of the NP size. Although the standard deviation in the measurements of these sizes is similar, as it can be observed in Table 1, the difficulty in distinguishing the CdTe QDs (due to the fact that these particles were found in sample S1 forming clusters or accumulations and not so much isolated) is reflected in the histogram in Fig. 3a, from which it is clear that a lower number of NPs were measured in sample S1. As expected, the histogram closer to a normal distribution corresponds to the Au NPs (sample S3) since their synthesis is better controlled and it does not present

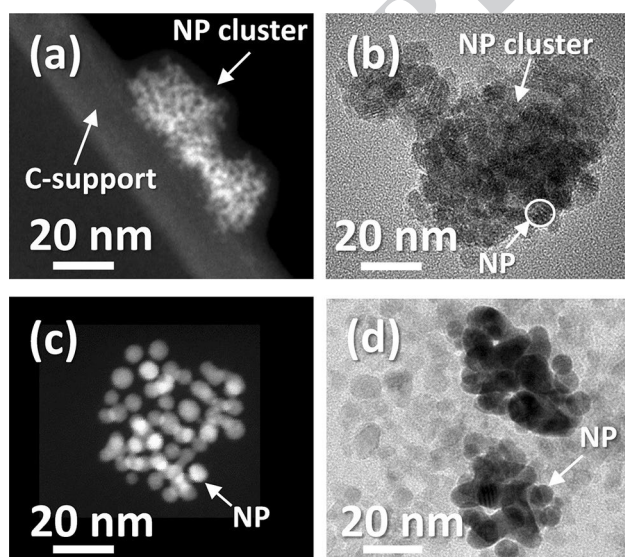


**Fig. 2** Accumulations of NPs in samples S1(a), S2(b), S3(c) and S4(d). Images for S1 and S3 correspond to STEM-HAADF mode, and images for S2 and S4 are taken in BF-TEM mode

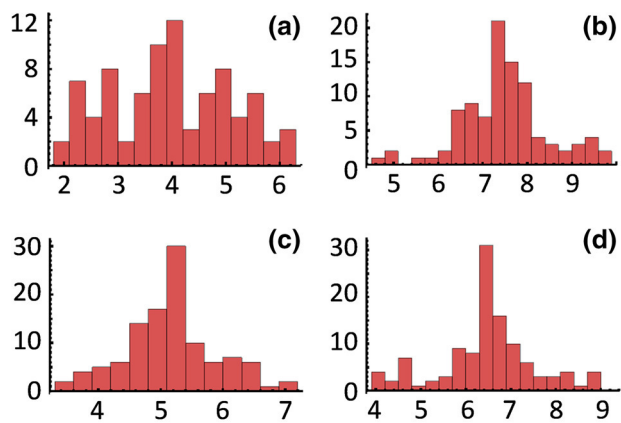


**Fig. 3** Histograms for NP sizes in samples S1(a), S2(b), S3(c), and S4(d). The horizontal axes indicate the NP size, in nm, while the vertical ones present the amount of NPs corresponding to each size range. The histogram bars correspond to increments in the size of 0.3 nm

295 magnetic behavior that leads to the cluster formations that  
296 would make difficult the measurement of the particle size.

297 Data in Table 1 together with the results from TEM  
298 images such as the ones presented in Fig. 2 indicate the NPs  
299 in this work could be a good choice as nanoparticle in medicine  
300 since the most attractive NPs for biomedical applications  
301 are those spherical and with sizes ranging from 2 to  
302 10 nm (Khan et al. 2018). Many body barriers fall in the  
303 sub-10-nm regime, but, on the other hand, NPs smaller than  
304 2 nm could considerably increase their toxicity.

305 In this sense, it can be mentioned that an appropriate  
306 method, easier than those based on hydrophobic routes, to  
307 prepare small soluble and functionalized NPs is to carry out  
308 a reduction in aqueous media using a strong reducing agent,  
309 like sodium borohydride, in the presence of strong capping  
310 ligands to control particle growth. Some advantages of this  
311 route reside in the possibility to choose a capping ligand that  
312 directly biofunctionalizes the NP or that facilitates its subse-  
313 quent biofunctionalization (Fratoddi 2018). This route also  
314 allows for the use of thiols as capping agents, due to the high  
315 affinity of this group for the NP surface (Dehn et al. 2018).

316 In this work, we have used this  $\text{NaBH}_4$  reduction reac-  
317 tion, adding both, the capping and the reduction agent in  
318 excess to promote the fast nucleation and successive growth  
319 to homogenize NP size. Increasing the nucleation step rate, a  
320 high proportion of nuclei will be formed before starting the  
321 growth step. This enhances the formation of small homoge-  
322 neous and spherical cores.

323 Figure 4 illustrates these ideas through HRTEM images  
324 for three types of NPs of this work. This figure does not  
325 show particles from sample S1 since it was not possible  
326 to achieve high-resolution conditions for NPs with CdTe  
327 cores. On the other hand, for the rest of samples, it was

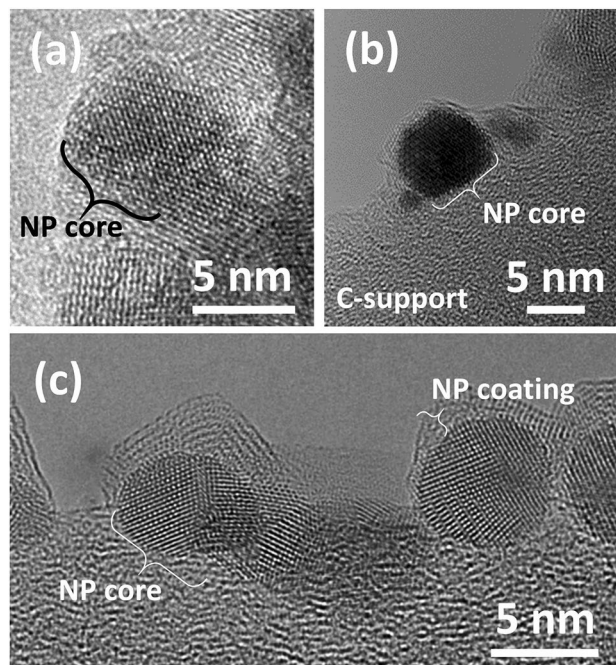


**Fig. 4** HRTEM images of individual NPs in samples S2(a), S4(b), and S3(c)

328 possible to observe NPs both inside the conglomerates  
329 (Fig. 4a) and isolated ones (Fig. 4b, c). Some NP core  
330 and coating layers, according with the ideas commented  
331 before, are also pointed out in this figure.

332 It is possible to obtain valuable information from the  
333 regions corresponding to the NP core using these HRTEM  
334 images. In this sense, the comparison of measurements  
335 for atomic planes distances with the ones theoretically  
336 expected for the different materials agrees with the affir-  
337 mation that the NPs cores are formed, indeed, by magnet-  
338 ite and/or gold. In this sense, measurements in images  
339 such as the one in Fig. 4a revealed experimental distances of  
340 2.9 Å, which agree with the expected distances between  
341 {220} atomic planes in magnetite particles (Haavik et al.  
342 2000). Figure 4b shows an example of a HRTEM image  
343 from a NP in sample S4. From this image and other analo-  
344 gous ones, it was possible to measure distances between  
345 atomic planes of 3.0 and 4.9 Å. This is in agreement with  
346 theoretical distances between the {220} and {111} fami-  
347 lies of planes of magnetite (2.97 and 4.85 Å, respectively)  
348 (Haavik et al. 2000), and also 2.4 Å, which can be associ-  
349 ated with the ones for the {111} planes in the case of Au  
350 (Richter et al. 2011). The HRTEM images of nanoparticles  
351 in Fig. 4d shows atomic distances of 2.1 and 2.4 Å, which,  
352 respectively, agree well with the spacing between {002}  
353 and {111} families of atomic planes for cubic Au (2.04  
354 and 2.35 Å, respectively) (Richter et al. 2011).

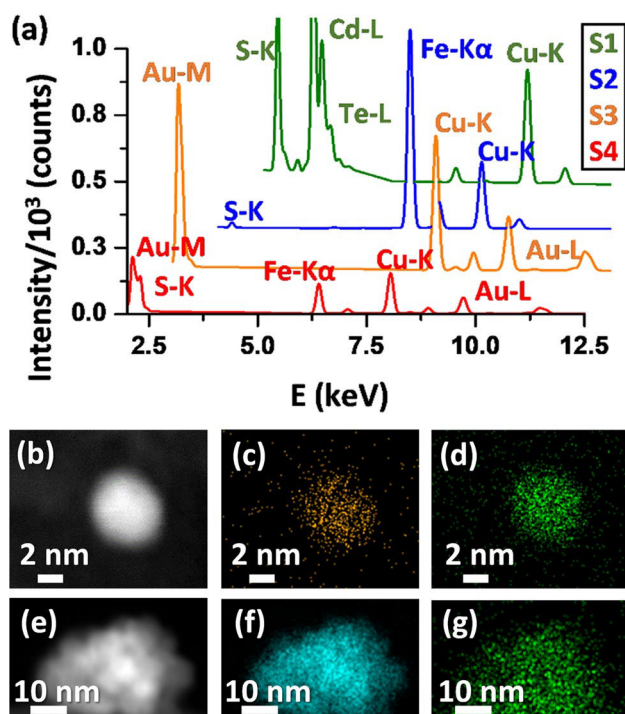


**Fig. 5** Punctual EDX spectra from NPs for all samples, with the corresponding element and X-ray peaks and color legend (a). Isolated NP in sample S3: HAADF image (b) and EDX maps for Au (c) and S (d). Agglomeration of NPs in sample S2: HAADF image (e) and EDX map for Fe (f) and S (g)

### 355 Compositional characterization

356 Figure 5 displays representative punctual EDX spectra for  
 357 NPs in the four samples (Fig. 5a), as well as EDX maps for  
 358 NPs (Fig. 5b–d) and accumulations of those (Fig. 5e–g). It  
 359 is possible to observe, in Fig. 5a, that the NPs have, indeed, the  
 360 expected chemical composition, revealing a sulfur K $\alpha$ -peak,  
 361 at 2.31 keV, in all cases (the gold M-peak, at 2.12 keV,  
 362 which appears in samples S3 and S4, partly overlap the sulfur  
 363 signal). This element is associated with the presence of  
 364 the glutathione shell around the NP core. Figure 5b presents  
 365 a HAADF image of a single NP (sample S3) for which an  
 366 EDX map has been recorded. Figure 5c reveals that this NP  
 367 has a gold core, while it is clear, according to Fig. 5d, that  
 368 the NP is totally covered with the S-containing compound  
 369 (glutathione). In this sense, it is also possible to show that  
 370 the glutathione coats the NPs even when they form conglomerates.  
 371 Figure 5e presents a HAADF image of a 30-nm-size  
 372 NP agglomeration. EDX maps of iron (Fig. 5f) and sulfur  
 373 (Fig. 5g) reveal that there is a homogeneous distribution of  
 374 magnetite and GSH, respectively, indicating that the syn-  
 375 thesis method leads to a majority of NPs in the sample with  
 376 the desired core and the glutathione layer. This result is also  
 377 observed in the other samples.

## Conclusions

A series of samples of GSH-capped NPs have been suc-  
 cessfully developed via chemical methods. The smallest and  
 rounder NPs, with the most clearly monocrystalline structure  
 of the core, have been obtained for gold-containing NPs.  
 On the other hand, worse results have been obtained for the  
 NPs with a CdTe core. (S)TEM-based techniques represent  
 a good choice to completely characterize these systems. The  
 spectroscopic techniques, combined with STEM images, are  
 especially indicated to reveal the sulfur in the glutathione  
 layer, which allows the visualization of this NP shell.

**Acknowledgements** The authors would like to acknowledge the SC-  
 ICYT and the CITIUS central services of the Universities of Cádiz  
 and Seville, respectively, which made possible the sample preparation  
 and TEM studies in this work. A. J. Santos would like to thank the  
 IMEYMAT Institute and the Spanish Ministry of Education and Cul-  
 ture for the concessions of Grants ICARO-173873 and FPU16-04386.  
 The authors would like to thank the Spanish Ministry of Economy  
 and Competitiveness for the economic support to the research project  
 MAT2015-67354-R (Program “Plan I+D+i”, subprogram “Retos”).

**Author contributions** RL and OB-M contributed to the study concep-  
 tion and design. Nanoparticle systems were synthesized by RL and  
 EF. (S)TEM microscopy techniques were carried out at three different  
 microscopes by AMB, JMM, AJS and FMM. OB-M and JMM, as  
 “investigadores principales” (main researchers) of Research Project  
 MAT2015-67,354-R, managed the necessary economical funds that  
 allowed this work. The first draft of the manuscript was written by  
 AMB and JMM and all authors commented on the previous versions  
 of the manuscript. All authors read and approved the final manuscript.

**Funding** This work has been funded by the Spanish Ministry of  
 Economy and Competitiveness, through the research project “*Síntesis  
 asistida por láser de nanopartículas ternarias: una ruta alternativa  
 para la fabricación de nuevos agentes de contraste multimodales para  
 el diagnóstico temprano del cáncer de mama*”, reference: MAT2015-  
 67354-R, of the Program “Plan I+D+i”, subprogram “Retos”.

**Data availability** Any of the data and material utilized to develop this  
 manuscript can be available at request of any researcher, via the cor-  
 responding author.

**Code availability** Not applicable.

## Compliance with ethical standards

**Conflict of interest** The authors declare that there is no conflict of in-  
 terest/competing interests associated with the work presented in this  
 manuscript.

## References

Amendola V, Pilot R, Frascioni M et al (2017) Surface plasmon reso-  
 nance in gold nanoparticles: a review. *J Phys Condens Matter*.  
<https://doi.org/10.1088/1361-648X/aa60f3>

- 425 Beato-López JJ, Fernández-Ponce C, Blanco E et al (2012) Preparation  
426 and characterization of fluorescent CdS quantum dots used for the  
427 direct detection of GsT fusion proteins. *Nanomater Nanotechnol.*  
428 <https://doi.org/10.5772/53926>
- 429 Beato-López JJ, Espinazo ML, Fernández-Ponce C et al (2017)  
430 CdTe quantum dots linked to Glutathione as a bridge for protein  
431 crosslinking. *J Lumin* 187:193–200. <https://doi.org/10.1016/j.jlumin.2017.03.012>
- 432 Birrenbach G, Speiser PP (1976) Polymerized micelles and their use  
433 as adjuvants in immunology. *J Pharm Sci* 65:1763–1766. <https://doi.org/10.1002/jps.2600651217>
- 434 Dehn MH, Arsenau DJ, Buck T et al (2018) Nature of magnetism in  
435 thiol-capped gold nanoparticles investigated with Muon spin rota-  
436 tion. *Appl Phys Lett.* <https://doi.org/10.1063/1.5017768>
- 437 Fernández-Ponce C, Muñoz-Miranda JP, de los Santos DM et al (2018)  
438 Influence of size and surface capping on photoluminescence and  
439 cytotoxicity of gold nanoparticles. *J Nanoparticle Res.* <https://doi.org/10.1007/s11051-018-4406-0>
- 440 Fratoddi I (2018) Hydrophobic and hydrophilic Au and Ag nanoparti-  
441 cles. Breakthroughs and perspectives. *Nanomaterials.* <https://doi.org/10.3390/nano8010011>
- 442 Gheibi Hayat SM, Darroudi M (2019) Nanovaccine: a novel approach  
443 in immunization. *J Cell Physiol* 234:12530–12536. <https://doi.org/10.1002/jcp.28120>
- 444 Griffin S, Masood MI, Nasim MJ et al (2018) Natural nanoparticles:  
445 a particular matter inspired by nature. *Antioxidants.* <https://doi.org/10.3390/antiox7010003>
- 446 Haavik C, Stølen S, Fjellvåg H et al (2000) Equation of state of mag-  
447 netite and its high-pressure modification: thermodynamics of the  
448 Fe-O system at high pressure. *Am Mineral* 85:514–523. <https://doi.org/10.2138/am-2000-0413>
- 449 Hochella MF (2002) There's plenty of room at the bottom: nanoscience  
450 in geochemistry. *Geochim Cosmochim Acta* 66:735–743. [https://doi.org/10.1016/S0016-7037\(01\)00868-7](https://doi.org/10.1016/S0016-7037(01)00868-7)
- 451 Hong R, Han G, Fernández JM et al (2006) Glutathione-mediated  
452 delivery and release using monolayer protected nanoparticle car-  
453 riers. *J Am Chem Soc* 128:1078–1079. <https://doi.org/10.1021/ja056726i>
- 454 Kairdolf BA, Smith AM, Stokes TH et al (2013) Semiconductor quan-  
455 tum dots for bioimaging and biondiagnostic applications. *Annu Rev*  
456 *Anal Chem* 6:143–162. <https://doi.org/10.1146/annurev-anchem-060908-155136>
- 457 Karley D, Gupta D, Tiwari A (2011) Biomarker for cancer: a great  
458 promise for future. *World J Oncol* 2:151–157. <https://doi.org/10.4021/wjon.v2i4.352>
- 459 Khan HA, Sakharkar MK, Nayak A et al (2018) Nanoparticles for  
460 biomedical applications: an overview. Elsevier Ltd., Amsterdam
- 461 Kreuter J (2009) Guest editorial: special issue for Prof. Dr. Peter Paul  
462 Speiser. *J Drug Target* 17:562–563. <https://doi.org/10.1080/10611860903090337>
- 463 Kumar A, Huo S, Zhang X et al (2014) Neupilin-1-targeted gold  
464 nanoparticles enhance therapeutic efficacy of platinum(IV) drug  
465 for prostate cancer treatment. *ACS Nano* 8:4205–4220. <https://doi.org/10.1021/nm500152u>
- 466 Kumari Y, Kaur G, Kumar R et al (2019) Gold nanoparticles:  
467 new routes across old boundaries. *Adv Colloid Interface Sci*  
468 274:102037. <https://doi.org/10.1016/j.cis.2019.102037>
- 469 Matsui I (2005) Nanoparticles for electronic device applications: a brief  
470 review. *J Chem Eng Japan* 38:535–546. <https://doi.org/10.1252/jcej.38.535>
- 471 Ramalingam V (2019) Multifunctionality of gold nanoparticles:  
472 plausible and convincing properties. *Adv Colloid Interface Sci*  
473 271:101989. <https://doi.org/10.1016/j.cis.2019.101989>
- 474 Righter K, Sutton S, Danielson L et al (2011) The effect of fO<sub>2</sub> on  
475 the partitioning and valence of v and Cr in garnet/melt pairs and  
476 the relation to terrestrial mantle v and Cr content. *Am Mineral*  
477 96:1278–1290. <https://doi.org/10.2138/am.2011.3690>
- 478 Le Trequesser Q, Sez nec H, Delville MH (2013) Functionalized nano-  
479 materials: their use as contrast agents in bioimaging: mono- and  
480 multi-modal approaches. *Nanotechnol Rev* 2:125–169. <https://doi.org/10.1515/ntrev-2012-0080>
- 481 Ventola CL (2017) Progress in nanomedicine: approved and investiga-  
482 tional nanodrugs. *PT* 42:742–755
- 483 Zhang Z, Huo F, Zhang X, Guo D (2012) Fabrication and size predic-  
484 tion of crystalline nanoparticles of silicon induced by nanogrind-  
485 ing with ultrafine diamond grits. *Scr Mater* 67:657–660. <https://doi.org/10.1016/j.scriptamat.2012.07.016>
- 486 Zhang Z, Guo D, Wang B et al (2015) A novel approach of high speed  
487 scratching on silicon wafers at nanoscale depths of cut. *Sci Rep*  
488 5:1–9. <https://doi.org/10.1038/srep16395>
- 489 Zhang Z, Cui J, Wang B et al (2017) A novel approach of mechani-  
490 cal chemical grinding. *J Alloys Compd* 726:514–524. <https://doi.org/10.1016/j.jallcom.2017.08.024>
- 491 Zhang Z, Cui J, Zhang J et al (2019) Environment friendly chemical  
492 mechanical polishing of copper. *Appl Surf Sci* 467–468:5–11. <https://doi.org/10.1016/j.apsusc.2018.10.133>
- 493 Zhang Z, Liao L, Wang X et al (2020) Development of a novel chemi-  
494 cal mechanical polishing slurry and its polishing mechanisms on a  
495 nickel alloy. *Appl Surf Sci* 506:144670. <https://doi.org/10.1016/j.apsusc.2019.144670>
- 496  
497  
498  
499  
500  
501  
502  
503  
504  
505  
506  
507  
508  
509  
510  
511  
512  
513  
514
- 515 **Publisher's Note** Springer Nature remains neutral with regard to  
516 jurisdictional claims in published maps and institutional affiliations.
- 517